Robust multiparameter method of evaluating the optical and thermal properties of a layered tissue structure using photothermal radiometry

Anna Matvienko,[1,2,*] Andreas Mandelis,[1,2] and Stephen Abrams[2]

[1]Center for Advanced Diffusion-Wave Technologies, Department of Mechanical and Industrial Engineering, University of Toronto, 5 King's College Road, Toronto, ON, M5S 3G8, Canada

[2]Quantum Dental Technologies Inc., 748 Briar Hill Ave, Toronto, ON, M6B 1L3, Canada

*Corresponding author: ann@mie.utoronto.ca

Received 31 March 2009; accepted 1 May 2009;
posted 19 May 2009 (Doc. ID 109398); published 5 June 2009

The thermal and optical properties of multilayered dental tissue structure, the result of the surface-grown prismless layer on enamel, were evaluated simultaneously using multiparameter fits of photothermal radiometry frequency responses. The photothermal field generated in a tooth sample with near-infrared laser excitation was described using a coupled diffuse-photon-density and thermal wave model. The optical (absorption and scattering) coefficients and thermal parameters (spectrally averaged infrared emissivity, thermal diffusivity and conductivity) of each layer, as well as the thickness of the upper prismless enamel layer, were fitted using a multiparameter simplex downhill minimization algorithm. The results show that the proposed fitting approach can increase robustness of the multiparameter estimation of tissue properties in the case of ill-defined multiparameter fits, which are unavoidable in *in vivo* tissue evaluation. The described method can readily be used for noninvasive *in vitro* or *in vivo* characterization of a wide range of layered biological tissues.

OCIS codes: 170.1850, 170.7050, 160.4760, 170.5270, 170.6935.

1. Introduction

The rapidly growing area of laser-based treatment and diagnosis requires accurate and precise *in vivo* evaluation of optical and thermal tissue properties. During the past decade, a host of *in vivo* methodologies were reported [1–3] for optical evaluation. These techniques apply the diffusion approximation of the transport theory [4] to extract from the measured optical reflectance or transmittance the optical properties of tissues: absorption coefficient, scattering coefficient, and the mean cosine of the scattering angle. Usually, semi-infinite homogeneous tissue is assumed, and the solution of the diffusion equation at the surface is calculated, subject to appropriate boundary conditions. However, many tissues are in fact multilayered. It has been shown that a single-layer approximation can lead to significant errors in the optical evaluation of layered tissues [5]. On the other hand, introducing several sets of optical coefficients for each layer and additional unknown thicknesses of the layers increases the complexity of the fitting procedure, where the number of constraints is smaller than the number of fitting parameters. The problem becomes ill-defined, i.e., several sets of parameters can describe the measured data equally well, thus questioning the uniqueness of the fits. In this case, the robustness of the fitting algorithm becomes of great importance. Several algorithms for

0003-6935/09/173193-12$15.00/0

extracting optical properties from the reflectance data of a two-layered system were investigated: the Marquardt–Levenberg nonlinear least squares algorithm [5,6], the Newton–Raphson and neural network algorithms [5], and simulated annealing minimization [7]. The described algorithms require an initial set of optical properties as input parameters. However, the main problem for the fitting analysis of biological tissues is that the true values of properties may vary greatly among the same type of tissues. In this case, the range of the initial properties can be considerably wide, compounded by algorithm sensitivity to changes in the initial guesses, which, in turn, affects the accuracy of the fits. High sensitivity to the initial parameters was reported for many algorithms, including the widely used Marquardt algorithm for multiparameter fits [7]. At the same time, the simulated annealing algorithm exhibited less dependence on the initial values. This algorithm belongs to the family of multiparameter minimization algorithms [8] searching the global minimum of functions (e.g., the minimum of the difference between experimental and theoretical curves). One of the most robust algorithms of this family, simplex downhill minimization [8], was compared to the ubiquitous Marquardt–Levenberg method for a wide range of initial data variations [9], showing a significantly greater degree of confidence in the fitted values than the latter. Indeed, for an initial guess variation between 5% and 40%, the failure rates for the Marquardt–Levenberg algorithm ranged from 0.1 to 91% (using the 99% confidence level from the resulting simplex distribution as a failure criterion).

The analysis of laser tissue irradiation becomes even more complicated due to involvement of the optical-to-thermal energy conversion and the necessity for the evaluation of thermal properties of tissues in addition to purely optical analysis.

During the past decade, besides purely optical methods, the so-called secondary-signal methods emerged. They usually depend on the secondary response in tissue generated due to light absorption, usually thermal [10] or acoustic signals [11], to measure tissue properties. The introduction of the secondary signal enhances the sensitivity and specificity of the measurements and increases the possibilities for the detection of early changes in tissues. The thermal and acoustic properties of tissues were used as known values in order to fit the thermal or acoustic signal in the aforementioned studies.

There are several studies on the measurement of purely thermal properties of biological tissues published in the literature [12,13]. Since the separate evaluation of thermal properties would increase the complexity of the investigation, the requirement for simultaneous measurement of both optical and thermal properties using the secondary-signal methods becomes attractive. However, considering the fact that biological tissues are usually layered structures and several sets of parameters must be introduced for each layer, the complexity of the fitting analysis increases dramatically in this case.

Frequency-domain photothermal radiometry (PTR) has recently shown the potential to provide simultaneous quantitative analysis of optical and thermal fields in multilayered dental tissue structures [14]. The technique has already shown its capabilities for the noninvasive optical evaluation of dental tissues [15]. The authors, however, considered a single-layer approximation and extracted optical properties only.

In this study, we apply frequency-domain PTR to simultaneously evaluate optical and thermal properties of teeth as layered structures. We measure the amplitude and phase of the PTR signal and apply the simplex downhill algorithm for the multiparameter fits of the relevant properties. The theoretical profiles are generated with the coupled diffuse-photon-density wave and thermal wave model for the multilayered turbid structures [14]. In the study, we considered enamel as a homogeneous layer. Since bulk enamel properties can be significantly different from the surface-grown prismless layer, the thickness of which can vary from 5 to 60 μm [16], in the present study the enamel layer was divided into two layers with separate sets of optical and thermal properties: a prismless enamel layer and a bulk enamel layer.

2. Theoretical Model of Coupled Diffuse Photon and Thermal-Wave Fields

A. Diffuse and Coherent Photon Fields

The theoretical approach is described in detail in our previous study [14]. We assume that a three-layered one-dimensional turbid structure is irradiated with laser light (Fig. 1). As a result of the incident radiation, a one-dimensional photon field density Ψ_t arises in the medium. It can be divided into two components:

$$\Psi_{t_i}(z;\omega) = \Psi_{c_i}(z;\omega) + \Psi_{d_i}(z;\omega), \tag{1}$$

where Ψ_{c_i} is the coherent photon density and Ψ_{d_i} is the diffuse photon density of the turbid medium. Here, the subscript i denotes each layer of the dental structure (Fig. 1). The first layer of the structure is

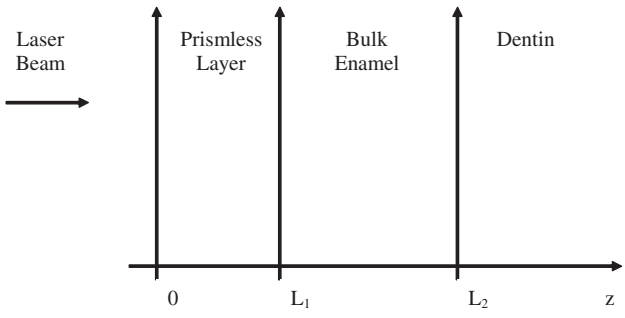

Fig. 1. Effective layered tooth structure for the PTR model.

the prismless enamel layer [17]. The second layer is healthy enamel, and the third layer is dentin.

The one-dimensional coherent photon-density field takes into account the reduction of the incident intensity due to the scattering and absorption [14]:

$$\Psi_{c_1} = \frac{I_0(1-R_1)\{\exp[-\mu_{t_1}z] + R_2\exp[-\mu_{t_1}(2L_1 - z)]\}}{1 - R_1R_2\exp[-2\mu_{t_1}L_1]},$$
$$\Psi_{c_2} = \frac{I_0(1-R_1)(1+R_2)\exp[-\mu_{t_1}L_1]\exp[-\mu_{t_2}(z-L_2)]}{1 - R_1R_2\exp[-2\mu_{t_1}L_1]},$$
$$\Psi_{c_3} = \frac{I_0(1-R_1)(1+R_2)\exp[-(\mu_{t_1}L_1 + \mu_{t_2}L_2)]\exp\{-\mu_{t_3}[z-(L_1+L_2)]\}}{1 - R_1R_2\exp[-2\mu_{t_1}L_1]}, \quad (2)$$

where I_0 is the laser intensity, R_1 is the reflectivity of the outermost turbid medium, R_2 is the reflectivity of the second layer, and

$$\mu_{t_i} = \mu_{a_i} + \mu_{s_i}. \quad (3)$$

Here, μ_{t_i} is the total attenuation coefficient of layer i, which includes the absorption coefficient μ_{a_i} (m^{-1}) and the scattering coefficient μ_{s_i} (m^{-1}) of the medium.

The one-dimensional diffuse-photon-density equation in frequency domain can be described as [18]

$$\frac{d^2}{dz^2}\Psi_{d_i}(z) - 3\mu_{a_i}\mu'_{t_i}\Psi_{d_i}(z) = -\frac{1}{D_i}G_i(z). \quad (4)$$

Here,

$$\mu_t' = \mu_a + (1-g)\mu_s \quad (5)$$

is the reduced attenuation coefficient. g is the mean cosine of the scattering angle. D represents the mean free path of photons limited by absorption and scattering. The function G_i represents a photon source [18]:

$$G_i(z) = \mu_{s_i}\left(\frac{\mu_{t_i} + g_i\mu_{a_i}}{\mu_{t_i} - g\mu_{s_i}}\right)\Psi_{c_i}. \quad (6)$$

The general solutions for the optical fields for each layer ($i = 1, 2, 3$), including coherent and diffuse components, can be written as

$$\Psi_{t_1}(z) = a_1\exp(Q_1z) + b_1\exp(-Q_1z) + I_{\text{eff}}(1 + C_{\mu 1})\{\exp[-\mu_{t_1}z] + R_2\exp[-\mu_{t_1}(2L_1 - z)]\}, \quad (7a)$$

$$\Psi_{t_2}(z) = a_2\exp[Q_2(z-L_1)] + b_2\exp[-Q_2(z-L_1)] + I_{\text{eff}}(1+R_2)(1+C_{\mu 2})\exp(-\mu_{t_1}L_1) \times \exp[-\mu_{t_2}(z-L_1)], \quad (7b)$$

$$\Psi_{t_3}(z) = b_3\exp\{-Q_3[z-(L_1+L_2)]\} + I_{\text{eff}}(1+R_2)(1 + C_{\mu 3})\exp[-(\mu_{t_1}L_1 + \mu_{t_2}L_2)]\exp\{-\mu_{t_3}[z - (L_1+L_2)]\}, \quad (7c)$$

where the integration constants due to the coherent field solutions are given by

$$C_{\mu_i} = \frac{3\mu_{s_i}(\mu_{t_i} + g\mu_{a_i})}{3\mu_{a_i}\mu_{t_i}' - \mu_{t_i}^2},$$
$$I_{\text{eff}} = \frac{I_0(1-R_1)}{1 - R_1R_2\exp(-2\mu_{t_1}L_1)}. \quad (8)$$

In Eqs. (7) Q_i are defined as $Q_i = \sqrt{3\mu_{a_i}\mu_{t_i}'}$. The third-kind boundary conditions at the air–tooth interface and the continuity of photon-density field and photon flux at the interfaces between solid layers are applied:

$$\Psi_{d_1}(0) = A\frac{d}{dz}\Psi_{d_1}(z)\Big|_{z=0},$$
$$\Psi_{d_1}(L_1) = \Psi_{d_2}(L_1),$$
$$D_1\frac{d}{dz}\Psi_{d_1}(z)\Big|_{z=L_1} = D_2\frac{d}{dz}\Psi_{d_2}(z)\Big|_{z=L_1},$$
$$\Psi_{d_2}(L_1+L_2) = \Psi_{d_3}(L_1+L_2),$$
$$D_2\frac{d}{dz}\Psi_{d_2}(z)\Big|_{z=L_1+L_2} = D_3\frac{d}{dz}\Psi_{d_3}(z)\Big|_{z=L_1+L_2}. \quad (9)$$

Here, the constant A is defined as [19]

$$A = 2D\left(\frac{1+r}{1-r}\right), \quad (10)$$

where r is the internal reflection of uniformly diffusing radiation, which depends on the index of

refraction of the sample [20]. Solving the system of the five boundary-condition equations, using the photon diffusion fields Eqs. (7) and the coherent field Eqs. (2), in Eq. (1), one can obtain the coefficients a_1, a_2, b_1, b_2, and b_3:

$$
\begin{aligned}
a_1 &= \frac{-d_1P - f_1N\exp(-2\mu_{t_1}L_1) - \frac{(2VF+G)\exp(Q_1L_1)}{(1+X_{12}-2VX_{12})}}{M - \frac{(1-X_{12}+2VX_{12})\exp(2Q_1L_1)}{(1+X_{12}-2VX_{12})}},\\
b_1 &= -a_1M - d_1P - f_1N\exp(-2\mu_{t_1}L_1),\\
a_2 &= b_2 + d_2Y_{22} + X_{12}a_1\exp(Q_1L_1) - X_{12}b_1\exp(-Q_1L_1)\\
&\quad + Y_{12}(f_1 - d_1)\exp(-\mu_{t_1}L_1),\\
b_2 &= VF - VX_{12}a_1\exp(Q_1L_1) + VX_{12}b_1\exp(-Q_1L_1),\\
b_3 &= -a_2X_{23}\exp(Q_1L_1) + b_2X_{23}\exp(-Q_1L_1)\\
&\quad + Y_{23}d_2\exp(-\mu_{t_2}L_2) - Y_{33}d_3. \qquad (11)
\end{aligned}
$$

Here, the parameters M, N, P, X, Y, and d are defined as

$$
\begin{aligned}
&M \equiv \frac{1 - Q_1A}{1 + Q_1A}, \quad N \equiv \frac{1 - \mu_{t_1}A}{1 + Q_1A}, \quad P = \frac{1 + \mu_{t_1}A}{1 + Q_1A},\\
&X_{ij} \equiv \frac{D_iQ_i}{D_jQ_j}, \quad Y_{ij} \equiv \frac{D_i\mu_{t_i}}{D_jQ_j},\\
&d_1 = C_{\mu_1}I_{\text{eff}}, \quad f_1 = d_1R_2,\\
&d_2 = C_{\mu_2}I_{\text{eff}}(1 + R_2)\exp(-\mu_{t_1}L_1),\\
&d_3 = C_{\mu_3}I_{\text{eff}}(1 + R_2)\exp[-(\mu_{t_1}L_1 + \mu_{t_2}L_2)]. \qquad (12)
\end{aligned}
$$

The coefficients F, G and V are defined as

$$
\begin{aligned}
F &= d_2\frac{\exp(-\mu_{t_2}L_2)(Y_{23} - 1)}{\exp(Q_2L_2)(X_{23} + 1)} + d_3\frac{\exp(1 - Y_{33})}{\exp(Q_2L_2)(X_{23} + 1)}\\
&\quad - d_2Y_{22} - (f_1 - d_1)Y_{12}\exp(-\mu_{t_1}L_1);\\
G &= -(f_1 + d_1)\exp(-\mu_{t_1}L_1) + d_1 + d_2Y_{22}\\
&\quad + (f_1 - d_1)Y_{12}\exp(-\mu_{t_1}L_1),\\
V &= \frac{1}{1 - \frac{(X_{23}-1)}{(X_{23}+1)}\exp(-2Q_2L_2)}. \qquad (13)
\end{aligned}
$$

B. Thermal-Wave Field

The analytical solution for the thermal-wave field is described in detail in our study [14]. The total diffuse photon density field Ψ_t is the source of the much more slowly propagating thermal-wave field given by

$$
\begin{aligned}
&\frac{d^2}{dz^2}T_i(z;\omega) - \sigma_i^2T_i(z;\omega) = -\eta_{\text{NR}}\frac{\mu_{a_i}}{\kappa_i}\Psi_{t_i}(z;\omega),\\
&\quad i = 1, 2, 3, \qquad (14)
\end{aligned}
$$

where

$$
\sigma_i = \sqrt{\frac{i\omega}{\alpha_i}} \qquad (15)
$$

is the thermal wave number (m^{-1}), which depends on the modulation frequency and on the thermal diffusivity α (m^2s^{-1}) of the ith layer. Here, η_{NR} is the nonradiative efficiency and κ_i is the thermal conductivity of the ith layer ($\text{Wm}^{-1}\text{K}^{-1}$).

The thermal-wave fields for each layer can be written in the form

$$
\begin{aligned}
T_1(z;\omega) &= A_1\exp(\sigma_1z) + B_1\exp(-\sigma_1z) + C_1\exp(Q_1z)\\
&\quad + D_1\exp(-Q_1z) + E_1\exp(-\mu_{t_1}z)\\
&\quad + F_1\exp[-\mu_{t_1}(2L_1 - z)], \qquad (16a)\\
T_2(z;\omega) &= A_2\exp[\sigma_2(z - L_1)] + B_2\exp[-\sigma_2(z - L_1)]\\
&\quad + C_2\exp[Q_2(z - L_1)] + D_2\exp[-Q_2(z - L_1)]\\
&\quad + E_2\exp[-\mu_{t_2}(z - L_1)], \qquad (16b)\\
T_3(z;\omega) &= B_3\exp\{-\sigma_3[z - (L_1 + L_2)]\}\\
&\quad + D_3\exp\{-Q_3[z - (L_1 + L_2)]\}\\
&\quad + E_3\exp\{-\mu_{t_3}[z - (L_1 + L_2)]\}. \qquad (16c)
\end{aligned}
$$

The coefficients C_i, D_i, E_i, and F_i are defined as

$$
\begin{aligned}
C_i &= -\frac{\eta_{\text{NR}_i}\mu_{a_i}}{\kappa_i(Q_i^2 - \sigma_i^2)}a_i, \quad i = 1, 2;\\
D_i &= -\frac{\eta_{\text{NR}_i}\mu_{a_i}}{\kappa_i(Q_i^2 - \sigma_i^2)}b_i, \quad i = 1, 2, 3;\\
E_i &= -\frac{\eta_{\text{NR}_i}\mu_{a_i}(1 + C_{\mu_i})}{\kappa_i(\mu_{t_i}^2 - \sigma_i^2)\,C_{\mu_i}}d_i, \quad i = 1, 2, 3;\\
F_i &= -\frac{\eta_{\text{NR}_i}\mu_{a_i}(1 + C_{\mu_i})}{\kappa_i(\mu_{t_i}^2 - \sigma_i^2)C_{\mu_i}}f_1. \qquad (17)
\end{aligned}
$$

Here, a_i, b_i, d_i, f_1 are given in Eqs. (11) and (12). To determine the coefficients A_i and B_i, the following boundary conditions are used:

$$
\begin{aligned}
&\kappa_1\frac{dT_1(z,\omega)}{dz}\bigg|_{z=0} = HT_1(0;\omega),\\
&T_1(L_1,\omega) = T_2(L_1,\omega),\\
&\kappa_1\frac{dT_1(z,\omega)}{dz}\bigg|_{z=L_1} = \kappa_2\frac{dT_2(z,\omega)}{dz}\bigg|_{z=L_1};\\
&T_2(L_1 + L_2,\omega) = T_3(L_1 + L_2,\omega),\\
&\kappa_2\frac{dT_2(z,\omega)}{dz}\bigg|_{z=L_1+L_2} = \kappa_3\frac{dT_3(z,\omega)}{dz}\bigg|_{z=L_1+L_2}. \qquad (18)
\end{aligned}
$$

As a result, the coefficients of the photothermal fields T_1, T_2, T_3 in Eqs. (16) can be found from the solution of the following system of equations:

$$
\begin{aligned}
&A_1(1-b_{01})-B_1(1+b_{01})=C_1(b_{01}-q_{11})+D_1(b_{01}+q_{11})\\
&\quad+E_1(b_{01}+m_{11})+F_1\exp(-\mu_{t_1}L_1)(b_{01}-m_{11}),\\
&A_1\exp(\sigma_1L_1)+B_1\exp(-\sigma_1L_1)-A_2-B_2=C_2+D_2+E_2\\
&\quad-C_1\exp(Q_1L_1)-D_1\exp(-Q_1L_1)\\
&\quad-(E_1+F_1)\exp(-\mu_{t_1}L_1);\\
&b_{12}A_1\exp(\sigma_1L_1)-b_{12}B_1\exp(-\sigma_1L_1)-A_2+B_2\\
&\quad=q_{22}C_2-q_{22}D_2-m_{22}E_2-q_{12}C_1\exp(Q_1L_1)\\
&\quad+q_{12}D_1\exp(-Q_1L_1)-m_{12}(F_1-E_1)\exp(-\mu_{t_1}L_1);\\
&A_2\exp(\sigma_2L_2)+B_2\exp(-\sigma_2L_2)+B_3\\
&\quad=-C_2\exp(Q_2L_2)-D_2\exp(-Q_2L_2)\\
&\quad-E_2\exp(-\mu_{t_2}L_2)-D_3-E_3,\\
&q_{23}A_2\exp(\sigma_2L_2)-q_{23}B_2\exp(-\sigma_2L_2)+B_3\\
&\quad=-q_{23}C_2\exp(Q_2L_2)+q_{23}D_2\exp(-Q_2L_2)\\
&\quad+m_{22}E_2\exp(-\mu_{t_2}L_2)-q_{33}D_3-m_{33}E_3,
\end{aligned}
\tag{19}
$$

where the following definitions are used:

$$
b_{ij}\equiv\frac{\kappa_i\sigma_i}{\kappa_j\sigma_j},\qquad q_{ij}\equiv\frac{\kappa_iQ_i}{\kappa_j\sigma_j},\qquad m_{ij}\equiv\frac{\kappa_i\mu_{t_i}}{\kappa_j\sigma_j}. \tag{20}
$$

The photothermal radiometric signal represents the overall Planck radiation emission integrated over the depth of the sample:

$$
\begin{aligned}
V_{\mathrm{PTR}}(\omega)=C(\omega)\mu_{\mathrm{IR}}\Bigg[&\int_0^{L_1}T_1(z,\omega)\exp(-\mu_{\mathrm{IR}}z)\mathrm{d}z\\
&+\int_{L_1}^{L_2}T_2(z,\omega)\exp(-\mu_{\mathrm{IR}}z)\mathrm{d}z\\
&+\int_{L_2}^{\infty}T_3(z,\omega)\exp(-\mu_{\mathrm{IR}}z)\mathrm{d}z\Bigg].
\end{aligned}
\tag{21}
$$

Here, μ_{IR} is the spectrally averaged effective infrared absorption/emission of the medium. Given the spectrally averaging approximation of $\mu_{\mathrm{IR}}(\lambda)$ implicit in this formula over the mid-IR detection bandwidth, for simplicity we set all $\mu_{\mathrm{IR}}(\lambda)$ coefficients equal (in the mean) across the entire half-space of interest $([0,L_1],[L_1,L_2],[L_2,\infty))$.

The instrumental transfer function $C(\omega)$ was calculated using a thermally thick glassy carbon sample (diameter 40 mm, thickness 10 mm, Grade GC-20SS, Tokai Carbon Co., Ltd., Japan) with known thermal properties ($k_s=5.8\,\mathrm{Wm^{-1}k^{-1}}$, $\alpha_s=4.8\times10^{-6}\mathrm{m^2/s}$) as a black semi-infinite reference. The PTR frequency-scanned signal $V_{\mathrm{carbon}}(\omega)$ from the glassy carbon was measured, and the data were fitted to the theoretical signal calculated for the semi-infinite opaque solid [18]:

$$
\begin{aligned}
V_{\mathrm{carbon}}(\omega)&=C(\omega)\int_0^{\infty}T_{\mathrm{carbon}}(z,\omega)\mathrm{d}z\\
&=C(\omega)\int_0^{\infty}\frac{I_0}{2\left(1+\frac{k_0\sigma_0}{k_s\sigma_s}\right)k_s\sigma_s}\exp(-\sigma_sz)\mathrm{d}z,
\end{aligned}
\tag{22}
$$

where k_0 and σ_0 are the thermal conductivity and the thermal-wave number of air, and k_s and σ_s are the thermal conductivity and the thermal-wave number of carbon glass. I_0, $\mathrm{Wm^{-2}}$, is the incident laser intensity. The only unknown parameter, the instrumental factor $C(\omega)$, was thus obtained from the fits.

The measured PTR signal has an oscillating character and can be represented as

$$
V_{\mathrm{PTR}}(\omega)=|V_{\mathrm{PTR}}(\omega)|\exp[i\varphi_{\mathrm{PTR}}(\omega)], \tag{23}
$$

where the amplitude and phase components are

$$
\mathrm{Amp}_{\mathrm{PTR}}(\omega)=|V_{\mathrm{PTR}}(\omega)|,\quad \mathrm{Phase}_{\mathrm{PTR}}(\omega)=\varphi_{\mathrm{PTR}}(\omega). \tag{24}
$$

It should be mentioned that in order to reduce the complexity of the computational fits to the three-layer description of the tooth structure, a two-layer approximation of the three-layer model was used in the fits of enamel data. This was done due to the fact that the bulk enamel thickness (>800 μm [21]) can be considered semi-infinite since its poor thermal and optical properties prevent the photothermal field from deep penetration beyond the enamel–dentin junction. In the two-layer approach, the tooth structure consisted of a finite prismless layer plus semi-infinite bulk enamel and no dentin layer, which simplified the analysis greatly. To verify the validity of the two-layer approximation, a set of simulations was performed, where the theoretical PTR signal was calculated with a three-layer model assuming that the third layer is dentin. The averaged literature values of the optical and thermal properties of enamel and dentin were used [15,22–24]. The simulations showed that the enamel thickness does not affect the calculated PTR curve in the frequency range above 8 Hz (Fig. 2), i.e., the dentin layer can be eliminated from consideration and the enamel layer can be considered as semi-infinite. This frequency range (>8 Hz) was used to collect data for best-fitting analysis.

It should be noted that the strict three-layer approach will be necessary for the subsequent analysis of the demineralized enamel, where the subsurface demineralized enamel layer appears [25]. For the purposes of the current two-layer study, we still used the three-layer equations and set the thickness of layer L_2 (bulk enamel) to an effective semi-infinite value (5 mm). This allowed us to keep consistency in using the same mathematical description and

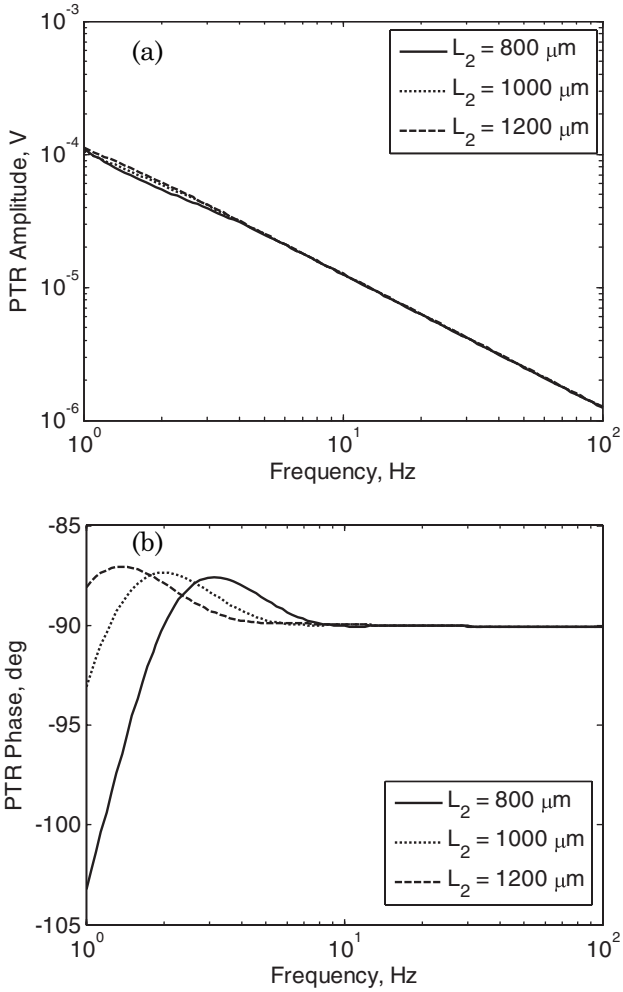

Fig. 2. PTR (a) amplitude and (b) phase calculated for various enamel thicknesses.

software package for our studies involving teeth demineralization [25].

3. Experimental Setup

The PTR experimental setup is shown in Fig. 3. A semiconductor laser diode emitting at 659 nm (Mitsubishi ML101J27, maximum power: 120 mW) was used as the source of the PTR signal. The diameter of the laser beam was approximately 3 mm to ensure the one-dimensionality of the photothermal field. A diode laser driver (Thorlabs, LDC 210) was triggered by the built-in function generator of the lock-in amplifier (EG&G 7265) to modulate the laser current harmonically. The modulated infrared PTR signal from the tooth was collected by two off-axis paraboloidal mirrors (Melles Griot 02POA017, rhodium coated) and focused onto a mercury cadmium telluride (HgCdTe or MCT) detector (Judson Technologies J15D12; spectral range, 2 to 12 μm; peak detectivity $D* \approx 5 \times 1010\,\mathrm{cm\,Hz^{1/2}W^{-1}}$ at approximately 12 μm). Before being sent to the lock-in amplifier, the PTR signal was amplified by a preamplifier (Judson Technologies PA-300). The lock-in amplifier was controlled by the computer via RS-232 ports.

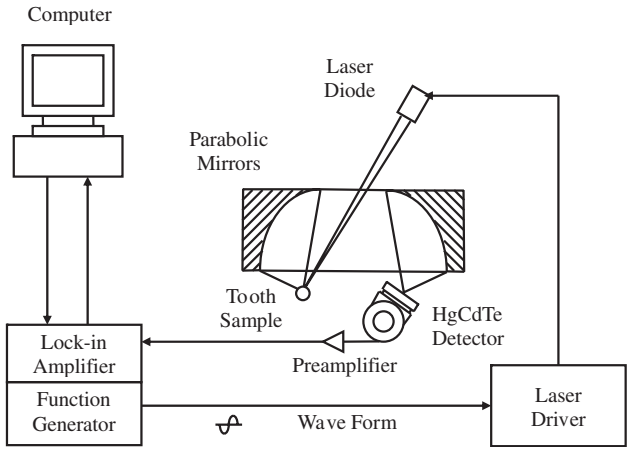

Fig. 3. Experimental setup.

A visually healthy tooth sample was mounted on a LEGO block base and placed on a micropositioning stage. The laser was turned on 10 min before measurements commenced, so that the sample surface was stabilized thermally.

The experiments consisted of frequency scans measuring the amplitude and the phase of the PTR signal by varying the frequency from 8 Hz to 100 Hz. The frequency range was segmented into equal intervals on a logarithmic scale by a data acquisition computer program and the frequency was automatically incremented to the next value after each measurement. There was a 15 s time delay between each frequency step to allow for thermal stabilization of the tooth surface.

Table 1. Upper and Lower Limits for the Initial Guess of Parameters (Bulk Enamel) [15,16,22–24]

	Lower Limit	Upper Limit	Mean Value and Range of Change
Absorption coefficient, μ_{a2}, $\mathrm{m^{-1}}$	1	100	50.5 ± 49.5
Scattering coefficient, μ_{s2}, $\mathrm{m^{-1}}$	4000	8000	6000.0 ± 2000.0
Thermal diffusivity, α_2, $\mathrm{m^2/s}$	4.2×10^{-7}	4.69×10^{-7}	$(4.445 \pm 0.245) \times 10^{-7}$
Thermal conductivity, λ_2, W/mK	0.910	0.926	0.918 ± 0.008
Nonradiative efficiency, η_{IR2}	0	1	0.5 ± 0.5
IR absorption coefficient, μ_{IR}, $\mathrm{m^{-1}}$	30,000	200,000	$115,000 \pm 85,000$
Heat transfer coefficient, H, $\mathrm{W/m^2K}$	0	1	0.5 ± 0.5
Prismless layer thickness, L_1, μm	5	60	32.5 ± 27.5
Mean cosine angle, g_2	0.60	0.98	0.79 ± 0.19
Reflectance of bulk enamel, R_2	0	1	0.5 ± 0.5

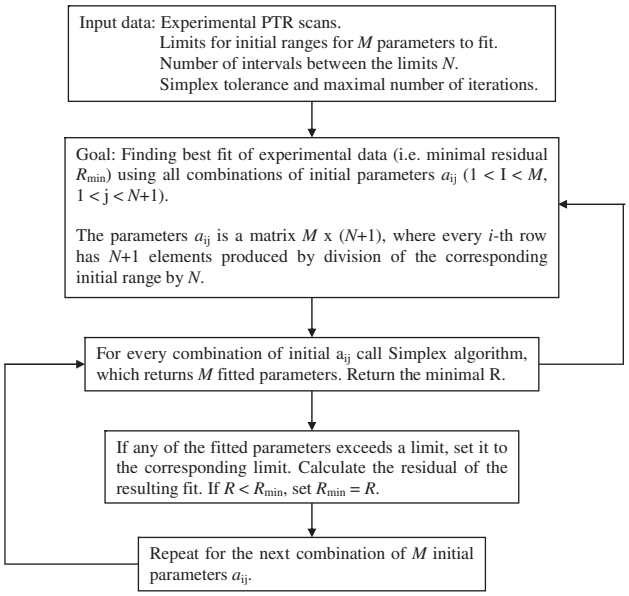

Fig. 4. Algorithm chart.

4. Multiparameter Fits to Experimental Data

A particular difficulty in the multiparameter fitting procedure is that the solution of the problem is usually not unique, i.e., multiple combinations of parameters can fit the data almost equally well. It is possible to apply additional constraints to the solution, e.g., measure (often destructively) some of the unknown parameters separately and then assume them as known values during the fits. However, this solution is difficult to implement for *in vivo* measurements in multilayered tissues. The properties of every layer can vary greatly among the same type of tissues, so the data obtained with other samples will not necessarily be the same as for the investigated tissue. At the same time, the application of several techniques even for the *in vivo* measurements of optical and thermal properties separately is undesirable from the clinical point of view. Practically, it would be much more convenient to apply one combined technique for the simultaneous estimation of the entire set of properties. Here, as was mentioned above, the robustness of the fitting algorithm, i.e., its independence from the initial guess of parameters, becomes extremely important. In our fitting procedure, we use the range of initial values within the limits based on the literature values [15,16,22–24] for every parameter (Table 1). The guess range for the optical absorption coefficient of the prismless layer was increased by 50% compared to bulk enamel, and for the optical scattering coefficient more than twice, since different orientations of the enamel crystals can significantly change the optical properties. The thermal diffusivity range was also significantly increased, since this parameter is highly sensitive to the composition of the layer structure.

During the fits, we divided the set of these ranges into equal steps and performed best fits for every

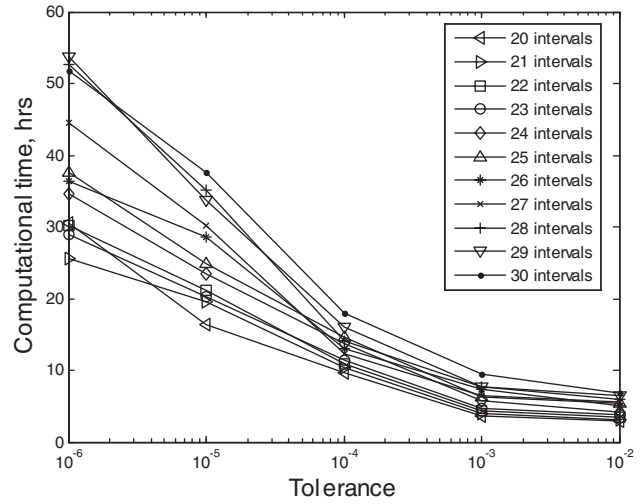

Fig. 6. Calculation time versus tolerance for various numbers of intervals N.

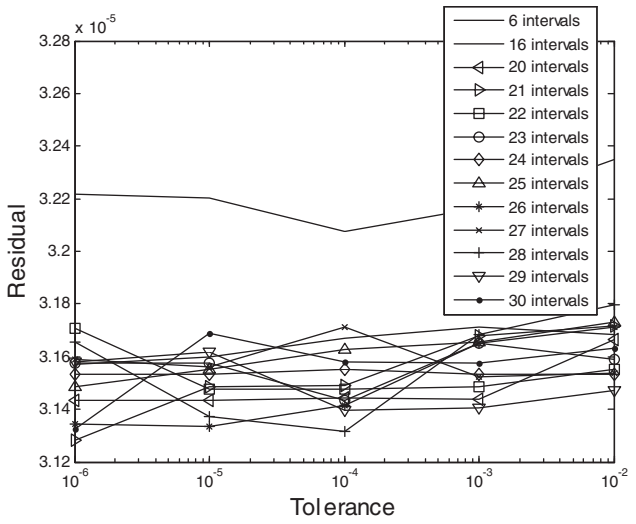

Fig. 5. Resulting residual versus tolerance of the simplex for various numbers of intervals N.

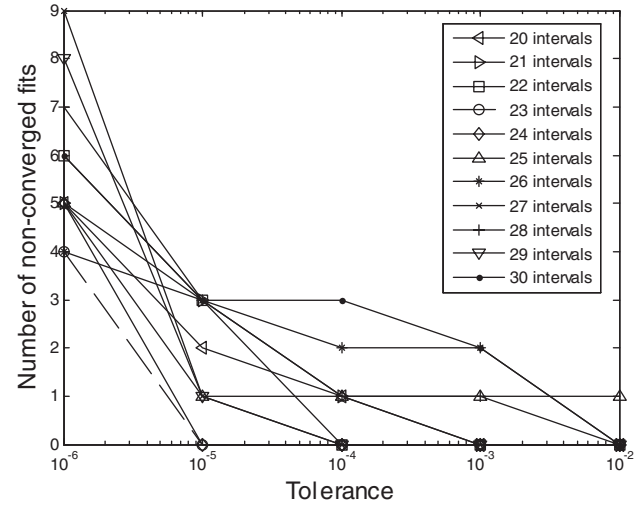

Fig. 7. Number of nonconverged fitting attempts versus tolerance of the fits. The curve corresponding to $N = 23$ is shown by a dashed line.

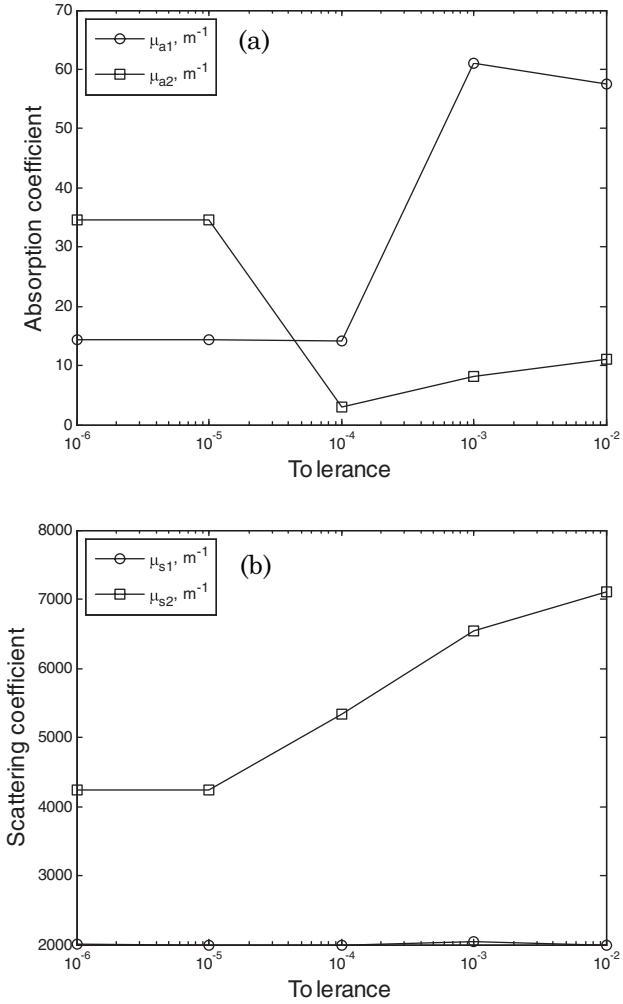

Fig. 8. Optical absorption and scattering coefficients versus tolerance. $N = 23$.

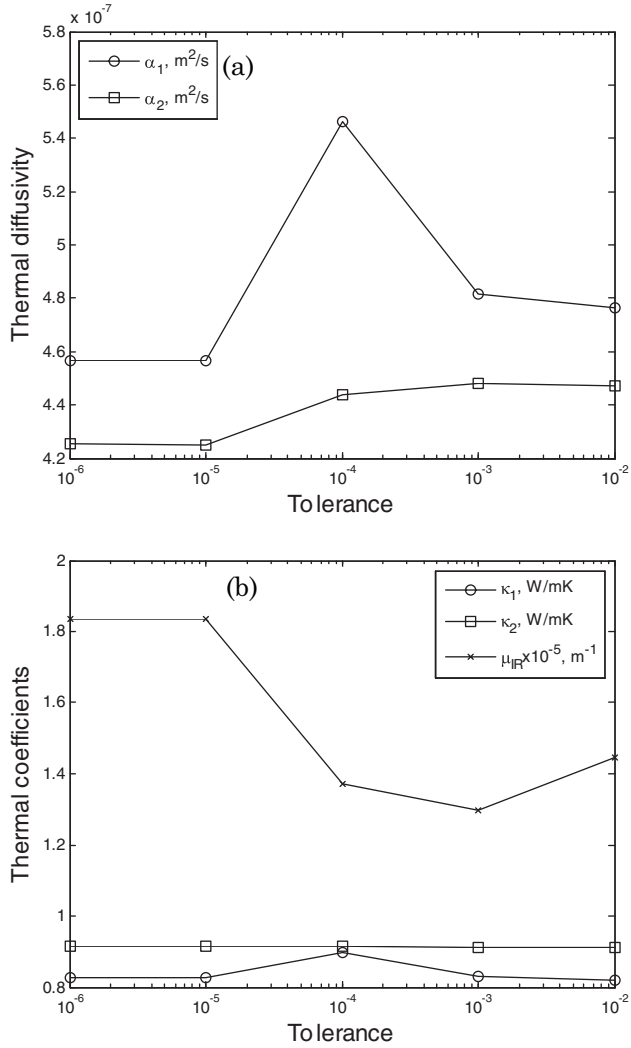

Fig. 9. Thermal diffusivities, thermal conductivities, and mean infrared absorption/emission coefficient versus tolerance. $N = 23$.

combination of points for every parameter (Fig. 4). These combinations of values become the initial guess sets for the fits. Thus, the dependence of the fitting results on the different combinations was thoroughly investigated before an actual set of resulting parameters was accepted as the final result.

The experimental PTR data were fitted using the simplex downhill algorithm for the multiparameter minimization [8]. Since the algorithm does not provide any restrictions to the fitting results, i.e., it can produce even negative numbers, only the resulting parameters that fell inside the initial range were considered. The amplitude and phase of the PTR signal were both fitted to the theory, and the combined residual represented the criterion for the best fits. The residual was defined as follows:

$$\mathrm{Res} = \frac{\sum_{n=1}^{n_{\max}} [\log_{10}(\mathrm{Amp_{Exp}}) - \log_{10}(\mathrm{Amp_{Theor}})]^2}{\sum_{n=1}^{n_{\max}} [\log_{10}(\mathrm{Amp_{Exp}})]^2} + \frac{\sum_{n=1}^{n_{\max}} [\mathrm{Phase_{Exp}} - \mathrm{Phase_{Theor}}]^2}{\sum_{n=1}^{n_{\max}} [\mathrm{Phase_{Exp}}]^2}, \quad (25)$$

where $\mathrm{Amp_{Exp}}$ and $\mathrm{Phase_{Exp}}$ are the measured PTR amplitude and phase, respectively, $\mathrm{Amp_{Theor}}$ and $\mathrm{Phase_{Theor}}$ are the calculated data, and $n_{\max}$ is the number of the frequency-scan points. Due to the large change in amplitude during experiments, the amplitude values were analyzed on a logarithmic scale. The simultaneous use of two signals, the salient feature of the frequency-domain methods, doubles the amount of information gathered in a single set of scans compared to time-domain techniques, increasing the fidelity of the fits.

The simplex downhill algorithm is described in detail elsewhere [8]. The fitting procedure was performed until the intrinsic tolerance of the fits was reached, or until the maximal number of iterations. The tolerance represents the change in the residual corresponding to the change in one of the fitting parameters. Once the change in any of the parameters stops decreasing the resulting residual (up to a certain number defined by the tolerance), the algorithm stops.

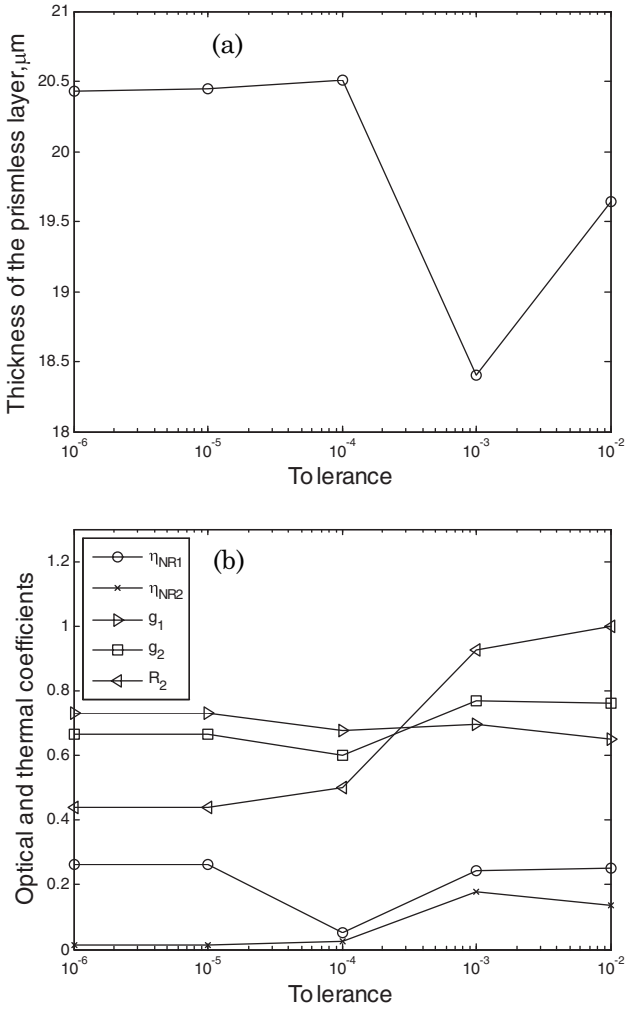

Fig. 10. Thickness, L_1, of the prismless layer and various optical and thermal coefficients versus tolerance. $N = 23$.

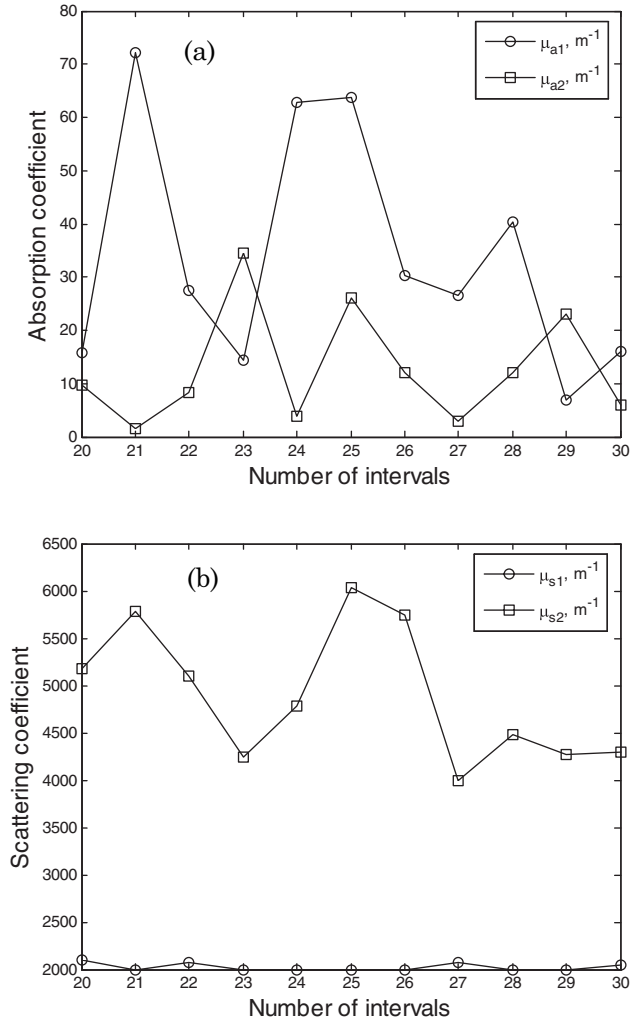

Fig. 11. Absorption and scattering coefficients versus number of intervals between the limits N.

5. Results and Discussion

The preliminary tests demonstrated that the quality of the fits increases with decreasing tolerance value (Fig. 5). However, the further decrease was limited by substantial increase in the computational time (Fig. 6).

In order to identify the optimal tolerance of the fits, the residual was compared for fits with different tolerance for several numbers of intervals between the parameter limits N. The number of unsuccessful fitting attempts, when convergence was not reached, is also shown for each set of parameters (Fig. 7). In this particular study, the maximum number of iterations 1×10^6 was chosen so the calculation time was reasonable (around 50 h or less per single fitting run).

It would be possible to decrease the number of nonconverged attempts by increasing the maximum number of iterations, but this increases the calculation time dramatically. It can be seen that for the smaller tolerances or larger number of intervals, i.e., larger number of trials, the nonconvergent runs appear more often (Fig. 7). At the same time, the resulting residual is not significantly smaller than that for the rest of the runs (Fig. 5). According to Fig. 5, the tolerance 1×10^{-5} gives stable residual values, i.e., the residual remains the same as with the tolerance values up to 10^{-6}. At the same time, the number of nonconvergent runs does not increase significantly compared to the tolerance 1×10^{-4} (Fig. 7). The decrease of the tolerance number up to 10^{-6} increased the calculation time (Fig. 6), significantly increased the number of nonconverged attempts, and did not decrease the residual, i.e., did not increase the quality of the fits. In addition, the investigation of the fits for $N = 23$, where the number of nonconverged attempts was 0 for the set of tolerance numbers from 10^{-2} to 10^{-5} and the number of nonconvergent attempts at 10^{-6} was 4, the smallest among all other runs (Fig. 7), which showed stabilization of the results with tolerances from 10^{-5} to 10^{-6} (Figs. 8–10). Therefore, the tolerance 10^{-5} was chosen for the further investigation of the robustness of the simplex fits, i.e., independence from the initial guess.

This investigation involved fitting the entire set of parameters several times with different number of intervals between the limits, i.e., with different

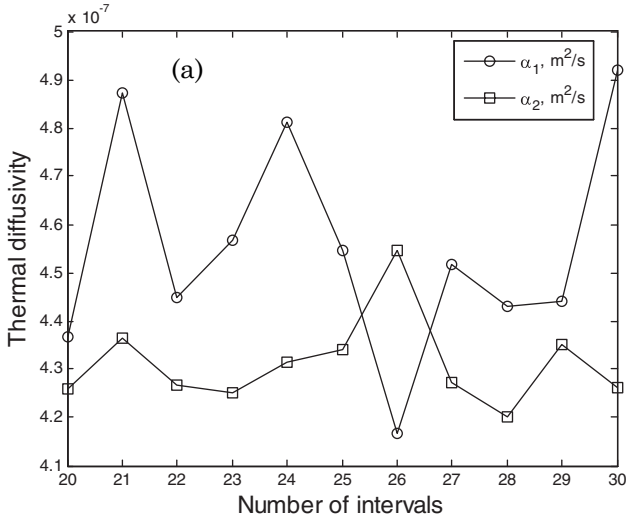

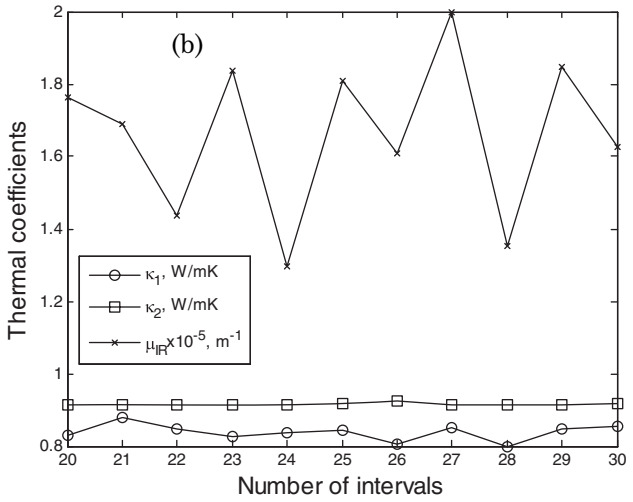

Fig. 12. Thermal diffusivities, thermal conductivities, and mean infrared absorption/emission coefficient versus number of intervals between the limits N.

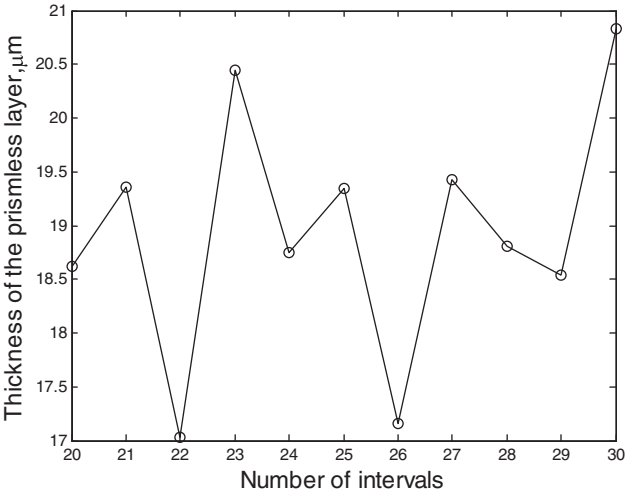

Fig. 13. Thickness, L_1, of the prismless layer versus number of intervals between the limits N.

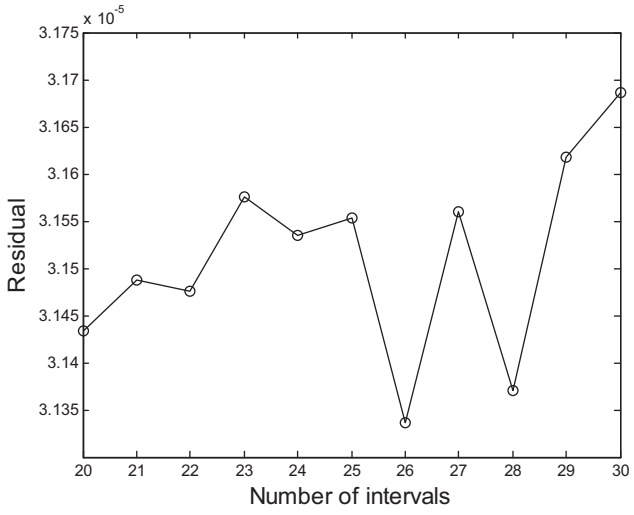

Fig. 14. Resulting residual versus number of intervals between the limits N.

refining steps of the grid of initial parameters. It is also seen (Fig. 5) that the main increase in the precision of the fits takes place when the number of

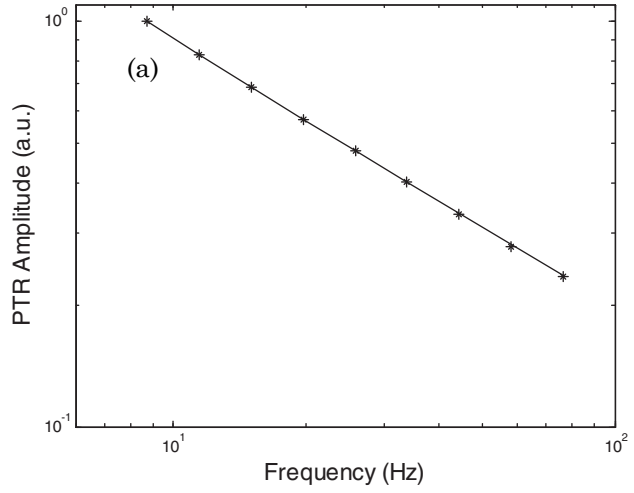

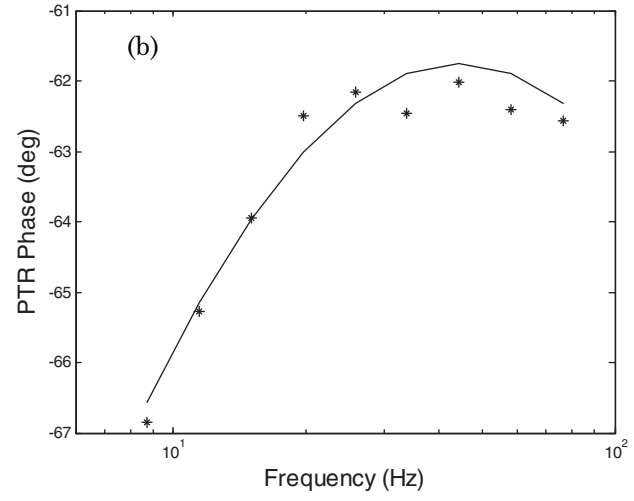

Fig. 15. Amplitude and phase for the PTR signal generated by a healthy tooth. Experimental data are represented with symbols. Calculated data are shown by a solid line.

Table 2. Results of the Fits Based on Calculations with the Number of Intervals N from 20 to 30, Simplex Downhill Tolerance $t = 10^{-5}$

	Mean Value	Range of Change	Initial Range of Change	Factor of Initial Range Reduction
Absorption coefficient, prismless layer, μ_{a1}, m^{-1}	34.20	65.04	150	2.3
Absorption coefficient, enamel, μ_{a2}, m^{-1}	12.73	32.98	100	3.0
Scattering coefficient, prismless layer, μ_{s1}, m^{-1}	2026.86	96.28	10,000	103.8
Scattering coefficient, enamel, μ_{s2}, m^{-1}	4900.21	2027.9	4000.0	1.9
Thermal diffusivity, prismless layer, α_1, m^2/s	4.55×10^{-7}	0.74×10^{-7}	4.8×10^{-7}	6.4
Thermal diffusivity, enamel, α_2, m^2/s	4.31×10^{-7}	0.34×10^{-7}	0.48×10^{-7}	1.4
Thermal conductivity, prismless layer, λ_1, W/mK	0.83	0.078	0.2	2.5
Thermal conductivity, enamel, λ_2, W/mK	0.91	0.012	0.016	1.3
Nonradiative efficiency, prismless layer, η_{IR1}	0.32	0.78	1	1.2
Nonradiative efficiency, enamel, η_{IR2}	0.16	0.44	1	2.2
IR absorption coefficient, μ_{IR}, m^{-1}	166,028	70,454	17,000	2.4
Heat transfer coefficient, H, W/m^2K	0.40	0.58	1	1.7
Prismless layer thickness, L_1, μm	18.93	3.8	55	14.4
Mean cosine angle, prismless layer, g_1	0.70	0.24	0.38	1.5
Mean cosine angle, enamel, g_2	0.71	0.14	0.38	2.7
Reflection coefficient, R_2	0.74	0.54	1	1.8

intervals is below $N = 20$. The further refinement of the initial grid gives stable values of the residual with no significant improvement. Therefore, the number of intervals between the limits of parameters was chosen to be $N \geq 20$. The upper bound for the number of intervals was limited to $N = 30$ due to the calculation time length issues discussed above.

Figures 11–14 represent the results of the fits as a function of the number of intervals N between the upper and lower limits of the parameters used to form the combinations of the initial guess sets. It can be seen that some of the parameters exhibit relatively stable values, almost independent of the initial guesses, and others vary considerably.

Table 2 summarizes the results of the fits. It can be seen that all the ranges between the minimum and maximum values of the resulting parameters are considerably smaller than the ranges of the initial guesses (see Table 1). The decrease in the deviation range up to 100 times demonstrates that the fitting algorithm can narrow the initial range down to relatively firm values which can accurately describe the properties of a sample, based on the best fits to the experimental scans. One of the most important parameters for the quantitative analysis of a layered structure, the thickness of the prismless layer L_1 (Fig. 13), exhibited very stable fitted values compared to the relatively wide range of the initial guess.

Figure 15 represents the final multiparameter fitting curves for the PTR signal generated by a healthy tooth, produced with the resulting parameters (Table 2) as initial values. The very good agreement between the experimental and the theoretical curves confirms the robustness of the approach for the simultaneous evaluation of the optical and thermal parameters of a multilayered tissue structure applied in our study. The results of this study have been further used in the *in vivo* optical and thermal evaluation of dental tissue structures during the demineralization process [25]. This type of analysis can allow for noninvasive detection of subsurface caries formation, thus opening a much needed possibility for preventive dental treatments.

6. Conclusions

The coupled diffuse-photon-density and thermal-wave model allowed for the theoretical description of the photothermal field generated in a sample following absorption of modulated near-infrared laser radiation. The optical (absorption and scattering) coefficients and thermophysical parameters (spectrally averaged infrared emissivity, thermal diffusivity and conductivity) of each layer, as well as the thickness of the upper prismless enamel layer, were fitted using the simplex downhill minimization algorithm. The results showed that the multiparameter fitting approach developed in this work can increase the robustness of the estimation of multiple tissue properties. The described method has been further used for noninvasive optical and thermal evaluation of dental tissue structures during an artificial demineralization process [25].

The authors are grateful to the Ontario Centers of Excellence (OCE) for a Market Readiness Award, the Natural Sciences and Engineering Research Council (NSERC), and the Ontario Premier's Discovery Award in Science and Engineering to A. Mandelis, which made this research possible. The authors thank A. Kogan, Technion—Israel Institute of Technology, for helpful discussions.

References

1. M. S. Patterson, B. Chance, and B. C. Wilson, "Time resolved reflectance and transmittance for the noninvasive measurement of tissue optical properties," Appl. Opt. **28**, 2331–2336 (1989).
2. A. Kienle, M. S. Patterson, N. Dognitz, R. Bays, G. Wagnieres, and H. van den Bergh, "Noninvasive determination of the optical properties of two-layered turbid media," Appl. Opt. **37**, 779–791 (1998).
3. F. Bevilacqua, D. Piguet, P. Marquet, J. D. Gross, B. J. Tromberg, and C. Depeursinge, "In vivo determination

of tissue optical properties: application to human brain," Appl. Opt. **38**, 4939–4950 (1999).
4. A. Ishimaru, "Diffusion of light in turbid material," Appl. Opt. **28**, 2210–2215 (1989).
5. T. J. Farrell, M. S. Patterson, and M. Essenpreis, "Influence of layered tissue architecture on estimates of tissue optical properties obtained from spatially resolved diffuse reflectometry," Appl. Opt. **37**, 1958–1972 (1998).
6. F. Martelli, S. Del Bianco, and G. Zaccanti, "Procedure for retrieving the optical properties of a two-layered medium from time-resolved reflectance measurements," Opt. Lett. **28**, 1236–1238 (2003).
7. G. Alexandrakis, T. J. Farrell, and M. S. Patterson, "Accuracy of the diffusion approximation in determining the optical properties of a two-layer turbid medium," Appl. Opt. **37**, 7401–7409 (1998).
8. W. H. Press, B. P. Flannery, S. A. Teukolsky, and W. T. Vetterling, *Numerical Recipes in C* (Cambridge University Press, 1988).
9. D. L. Buckley, R. W. Kerslake, S. J. Blackband, and A. Horsman, "Quantitative analysis of multi-slice Gd-DTPA enhanced dynamic MR images using an automated Simplex minimization procedure," Magn. Res. Med. **32**, 646–651 (1994).
10. S. A. Prahl, I. A. Vitkin, U. Bruggemann, B. C. Wilson, and R. R. Anderson, "Determination of optical properties of turbid media using pulsed photothermal radiometry," Phys. Med. Biol. **37**, 1203–1217 (1992).
11. A. A. Oraevsky, S. L. Jacques, and F. K. Tittel, "Measurements of tissue optical properties by time-resolved detection of laser-induced transient stress," Appl. Opt. **36**, 402–415 (1997).
12. S. A. Telenkov, J.-I. Youn, D. M. Goodman, A. J. Welch, and T. E. Milner, "Non-contact measurement of thermal diffusivity in tissue," Phys. Med. Biol. **46**, 551–558 (2001).
13. J. L. Pichardo-Molina, G. Gutierrez-Juarez, R. Huerta-Franco, M. Vargas-Luna, P. Cholico, and J. J. Alvarado-Gil, "Open photoacoustic cell technique as a tool for thermal and thermo-mechanical characterization of teeth and their restorative materials," Int. J. Thermophys. **26**, 243–253 (2005).
14. A. Matvienko, A. Mandelis, R. J. Jeon, and S. H. Abrams, " Theoretical analysis of coupled diffuse-photon-density and thermal-wave field depth profiles photothermally generated in layered turbid dental structures," J. Appl. Phys. **105**, 102022 (2009).
15. L. Nicoalides, C. Feng, A. Mandelis, and S. H. Abrams, "Quantitative dental measurements by use of simultaneous frequency-domain laser infrared photothermal radiometry and luminescence," Appl. Opt. **41**, 768–777 (2002).
16. A. Kakaboura and L. Papagiannoulis, "Bonding of resinous materials on primary enamel, in dental hard tissues and bonding," in *Interfacial Phenomena and Related Properties*, T. Eliades and C. Watts, eds. (Springer, 2005) pp. 35–51.
17. M. Fava, I. S. Watanabe, F. Fava-de-Moraes, and L. R. R. S. da Costa, "Prismless enamel in human non-erapted deciduous molar teeth: a scanning electron microscopy study," Rev. Odontol. Univ. Sao Paulo **11**, 239–243 (1997).
18. A. Mandelis, *Diffusion Wave Fields: Mathematical Methods and Green Functions* (Springer, 2001), Chap. 10.
19. Z. A. J. Groenhuis, H. A. Ferwerda, and J. J. Ten Bosch, "Scattering and absorption of turbid materials determined from reflection measurements. 1: Theory," Appl. Opt. **22**, 2456–2462 (1983).
20. R. R. Anderson, H. Beck, U. Bruggemann, W. Farinelli, S. L. Jacques, and J. A. Parrish, "Pulsed photothermal radiometry in turbid media: internal reflection of backscattered radiation strongly influences optical dosimetry," Appl. Opt. **28**, 2256–2262 (1989).
21. T. M. Smith, A. J. Olejniczak, D. J. Reid, R. J. Ferrell, and J. J. Hublin, "Modern human molar enamel thickness and enamel-dentin junction shape," Arch. Oral Biol. **51**, 974–995 (2006).
22. D. Fried, R. E. Glena, J. D. B. Featherstone, and W. Seka, "Nature of light scattering in dental enamel and dentin at visible and near-infrared wavelengths," Appl. Opt. **34**, 1278–1285 (1995).
23. M. Braden, "Heat conduction in normal human teeth," Arch. Oral Biol. **9**, 479–486 (1964).
24. W. S. Brown, W. A. Dewey, and H. R. Jacob, "Thermal properties of teeth," J. Dent. Res. **49**, 752–755 (1970).
25. A. Matvienko, A. Mandelis, A. Hellen, R. J. Jeon, S. H. Abrams, and B. T. Amaechi, "Quantitative analysis of incipient mineral loss in hard tissues," Proc. SPIE **7166**, 71660C (2009).